Novel BDD-loaded Bimetallic Phosphide Electrodes Enable Interesting Bifunctional Seawater Electrolysis

Xiaolei YE ^{1,2}, Genjie CHU ^{1,2}, Jiyun GAO ^{1,3}, Ming HOU ^{1,2*}, Shenghui GUO ^{1,2*}, Yunchuan LI ^{1,2}, Ziqi ZHOU ^{1,2}, Mingxu LI ^{1,2}, Li YANG ^{1,2}, Pascal Briois ⁴

- 1. Faculty of Metallurgical and Energy Engineering, Kunming University of Science and Technology, Kunming 650093, China
- State Key Laboratory of Complex Nonferrous Metal Resources Clean Utilization;
 Faculty of Metallurgical and Energy Engineering, Kunming University of Science and Technology, Kunming 650093, China
- 3. School of Chemistry and Environment, Yunnan Minzu University, Kunming 650093, China
- 4. FEMTO-ST Institute (UMR CNRS 6174), UBFC/UTBM. Site de Montbéliard, F-90010 Belfort-France

Corresponding author: Ming HOU (houmingkmust@163.com); Shenghui GUO (20040051@kust.edu.cn)

Abstract: The direct electrolysis of seawater for the production of green hydrogen energy is an economically attractive approach. However, this technique confronts technical problems because to the oxygen evolution reaction (OER) weak stability and inadequate selectivity due to competition with the chlorine evolution process. This work focuses on improving the stability of the electrode and electrolysis efficiency. The phosphating NiCoP active layer with 3D porous morphology was created by electrodeposition on the B-doped diamond (BDD) as an electrode inspired by the bifunctional catalysis strategy. The successfully constructed unique cube-onnanosheets structure in the NiCoP active layer enables the electrode to exhibit excellent electrocatalytic performance. The porous NiCoP/BDD (Por-NiCoP/BDD) electrodes showed good catalytic activity in alkaline-simulated seawater with the OER and hydrogen evolution reaction (HER) overpotentials of 400 and 261 mV, respectively, at a current density of 100 mA cm⁻². More importantly, the electrode exhibits interesting stability of the catalytic performance and structural in alkalinesimulated seawater electrolysis, with the current density decaying by only 1.52 % and 4.06 % after OER and HER processes for 50 h, respectively. This work expands the valuable application scenarios of BDD electrode and provides novel ideas for the development of seawater electrolysis.

Key word: Seawater electrolysis, B-doped diamond (BDD) electrode, Bifunctional catalysis, Transition metal phosphides, High stability and selectivity electrode

1. Introduction

The energy crisis triggered by global environmental changes and the immoderate use of non-renewable energy source has received significant attention. A consensus regarding the development of efficient, and clean new energy sources for sustainable development has been reached [1-3]. Hydrogen is considered an ideal new energy source with the properties of environmentally friendly and high energy density of up to 142 MJ, which is expected to replace traditional fossil fuel [4-6]. Development of efficient and economical hydrogen production technologies has become a major research topic [6-8]. Hydrogen production from freshwater electrolysis is a green approach that has been heavily reported in the past decade. However, freshwater, an indispensable resource for life, accounts for only 3.5% of global water resources, and a large portion is located in polar glaciers. Seawater, one of the richest natural resources on earth, accounts for 96.5% of the global water resources, is readily available for making seawater electrolysis more likely to be used as a long-term water electrolysis process for hydrogen production [9]. Nevertheless, electrolyzing seawater for hydrogen production still experiences technical challenges, such as electrode stability and the competition between the OER and the chlorine evolution reaction [10]. Additionally, electrolysis of seawater requires overcoming a higher anode OER energy barrier compared with freshwater [11]. Consequently, the development of stable electrodes loaded with dual electrocatalysts with excellent catalytic activity in the complex seawater environment is crucial for hydrogen production to achieve the sustainable development of green hydrogen energy. Current research on electrodes is focused on improving retarded HER and OER kinetics, reducing excessive overpotential in non-acidic ambient. Developing novel bifunctional catalysts with good performance that can balance OER and HER activities under moderate electrochemical conditions for seawater electrolysis is fundamentally and practically crucial.

Among the non-platinum-group-metal bifunctional catalysts, transition metal selenides (TMS) are considered as promising HER catalysts and OER precatalysts

because of their developed oxidized surfaces with active substances that catalyze water electrolysis [12]. However, the practical application of TMS is less satisfactory because it is prone to failure in complex seawater environments [13-14]. Currently, transition metal phosphides (TMPs) have attracted widespread attention due to their excellent HER performance, which benefits from the proton/hydride-acceptor sites on the material surface, producing a "synergistic effect" [15-16]. In particular, the synergistic effect of bimetallic phosphides catalysts such as FeCoP [17], NiCoP [18-20], and CoMoP [21], is more obvious, which greatly promotes the HER catalytic performance. Typically, this active catalyst is attached to nickel foam to form an electrode for seawater electrolysis. However, electrodes based on nickel foam face challenges in long-term stability in complex seawater [22-23]. It is well known that boron doped diamond (BDD) is an excellent semiconductor with strong corrosion resistance and long-term stability, which has made outstanding contributions in the field of electrochemistry. Thanks to this, it has a higher stability compared to conventional nickel foam in complex solutions, especially alkaline solutions [24-25]. Compounding efficient catalysts with BDD as a substrate is a piece of research worth exploring.

Herein, we created a variety of 3D porous hierarchical nano-island-like CoNiP/CoP multi-phase heterostructures with various Ni/Co ratios on BDD via phosphorizing a NiCo precursor produced by electrodeposition. The porous morphology and elemental distribution of the electrode surface were characterized by scanning electron microscope (SEM) and energy dispersive spectrometry (EDS. Transmission electron microscope (TEM) was used to observe the microcrystalline structure and properties of the sample. The catalyst material composition and chemical bonding were also analyzed through X-ray diffraction (XRD) and X-ray photoelectron spectroscopy (XPS). Finally, the HER, OER and long-term stability performance of the Por-NiCoP/BDD electrode were characterized by electrochemical tests in a alkaline-simulated seawater.

2. Materials and methods

2.1 Methods of sample preparation

All reagents were acquired commercially and utilized without additional purification, including nickel sulfate hexahydrate (NiSO₄·6H₂O), Co sulfate heptahydrate (CoSO₄·7H₂O), ammonium sulfate ((NH₄)₂SO₄), ammonia (NH₄OH), sodium hypophosphite monohydrate (NaH₂PO₂·H₂O), dilute hydrochloric acid (HCl), caustic soda (NaOH), anhydrous ethanol (C₂H₅OH), and sodium chloride (NaCl). BDD (10 mm \times 10 mm \times 0.65 mm), stainless steel plate (self-made), and deionized water were also used.

An electrodeposition approach was used to create a group of multi-phases NiCoP heterostructures produced on BDD, which was then phosphorized. Before depositing, the BDDs electrode was cleaned in 1 M HCl and 1 M NaOH by ultrasonic cleaning for 30 min in sequence. Subsequently, the BDDs were rinsed with anhydrous ethanol and deionized water in sequence, and the cleaned BDDs were dried at 60 °C to exclude the influence of impurities on the depositing process. The cleaned BDD surface was firstly electrodeposited with a porous NiCo layer by a DC power supply at the constant current to 0.5 A. The electrolyte composition was 100 mL of a mixed solution of NiSO₄·6H₂O, CoSO₄·7H₂O, 1 M (NH₄)₂SO₄, and ammonia (contents of 5%, 10%, and 20%). The concentration ratio of NiSO₄·6H₂O and CoSO₄·7H₂O was 0.67, 1.5, and 4 (0.04 M: 0.06 M, 0.06 M: 0.04 M, and 0.1 M: 0.025 M). During electrodeposition, the BDD and stainless steel plate were used as the cathode and anode, respectively. The geometric area of the BDD immersed in the electrolyte during electrodeposition was 0.5×1.0 cm⁻². The electrodeposition was carried out at 25 °C for 60 min, and the Por-NiCo/BDD electrode was finally obtained. During the phosphatization, Por-NiCo/BDD was placed in the core of a tube furnace, with 1.0 g NaH₂PO₂H₂O placed upstream and near the Por-NiCo/BDD. The furnace was heated to 450 °C at a rate of 5 °C /min in an Ar atmosphere and maintained for 2 hours. After the heat treatment, the furnace was naturally cooled to room temperature. Finally, the metallic NiCo precursor was converted into NiCoP after phosphorization. Fig. 1 depicts the preparation process.

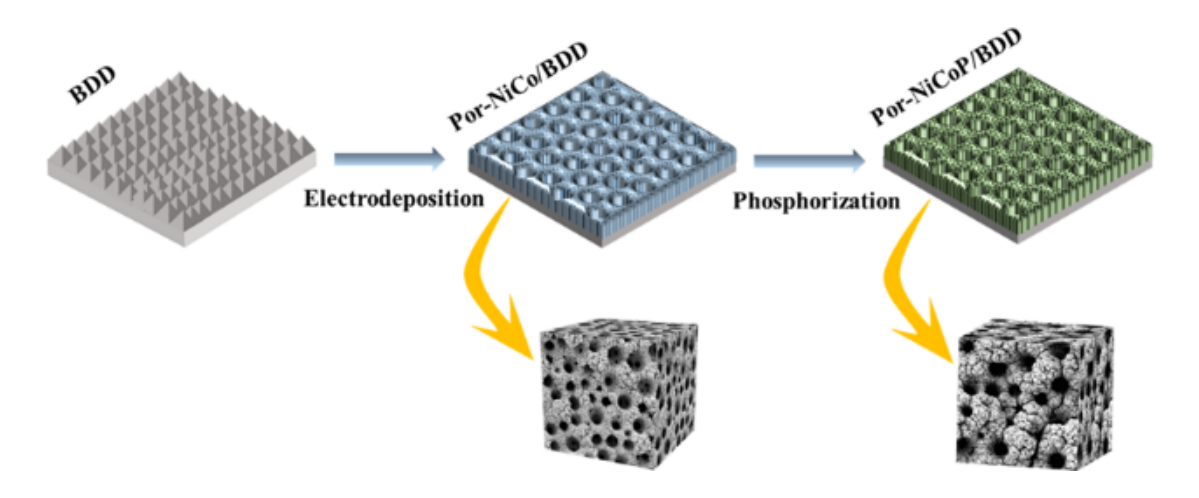


Fig. 1. Por-NiCoP/BDD electrode preparation diagram.

2.2 Samples characterization

Transmission Electron Microscopy (TEM) and Field Emission Scanning Electron Microscope (FESEM) as well as Energy Disperse Spectroscopy (EDS) were recorded on a JEM-2100 microscope TEM and JSM-5610L FESEM, respectively. XRD patterns were obtained on a BRUKER D8 diffractometer with Cu Kα radiation. XPS was investigated by a Thermo Fisher Scientific, which operates under the high vacuum (2×10⁻⁷ mbar) with aluminum Kα monochromatized radiation at the 1486.7 eV X-ray photon source. XPS data were analyzed using Thermo Advantage and energy corrections on high-resolution scans were calibrated by reference the C 1s peak of adventitious carbon to 285.0 eV.

2.3 Electrochemical measurements

The electrochemical measurements of as-prepared samples, including CV, LSV, EIS, HER, OER, and chrono-current (*i-t*) were carried out via an electrochemical workstation (CH1760e) in 1 M KOH and alkaline-simulated seawater containing a mixture of 1 M KOH and 3.5% NaCl at room temperature. The as-prepared samples as the working electrode, graphite rod as the counter electrode, and Hg/HgO or Ag/AgCl as the reference electrode were used in testing. Ag/AgCl reference electrode was used for HER and OER tests. Hg/HgO reference electrode was used for CV test. The test details were described in the Results and Discussion section.

3. Results and Discussion

The optimum Ni/Co concentration deposition conditions were determined based on the HER and OER performance of each electrode sample tested in 1 M KOH solution after deposition. The catalytic performance of the Por-NiCo/BDD electrode deposited in different Ni/Co concentrations is shown in Fig. 2. The linear scanning voltammetric (LSV) curves of the HER and OER tests in 1 M KOH solution for the Por-NiCo/BDD electrode samples deposited in the different Ni/Co concentrations (Figs. 2a-b). Fig. 2c shows the overpotential of HER and OER for each Por-NiCo/BDD electrodes at 50 and 100 mA cm⁻² current density. From Fig. 2c, the Ni/Co concentration in electrolyte affected the electrocatalytic performance of the Por-NiCo/BDD electrode. The Por-NiCo/BDD electrode deposited in the Ni/Co concentration ratio of 1.5 exhibited the smallest HER and OER overpotentials, indicating that this electrode has the best electrocatalytic performance. Therefore, the Por-NiCo/BDD electrodes mentioned below in this work were prepared at a Ni/Co concentration ratio of 1.5 without any other special instructions.

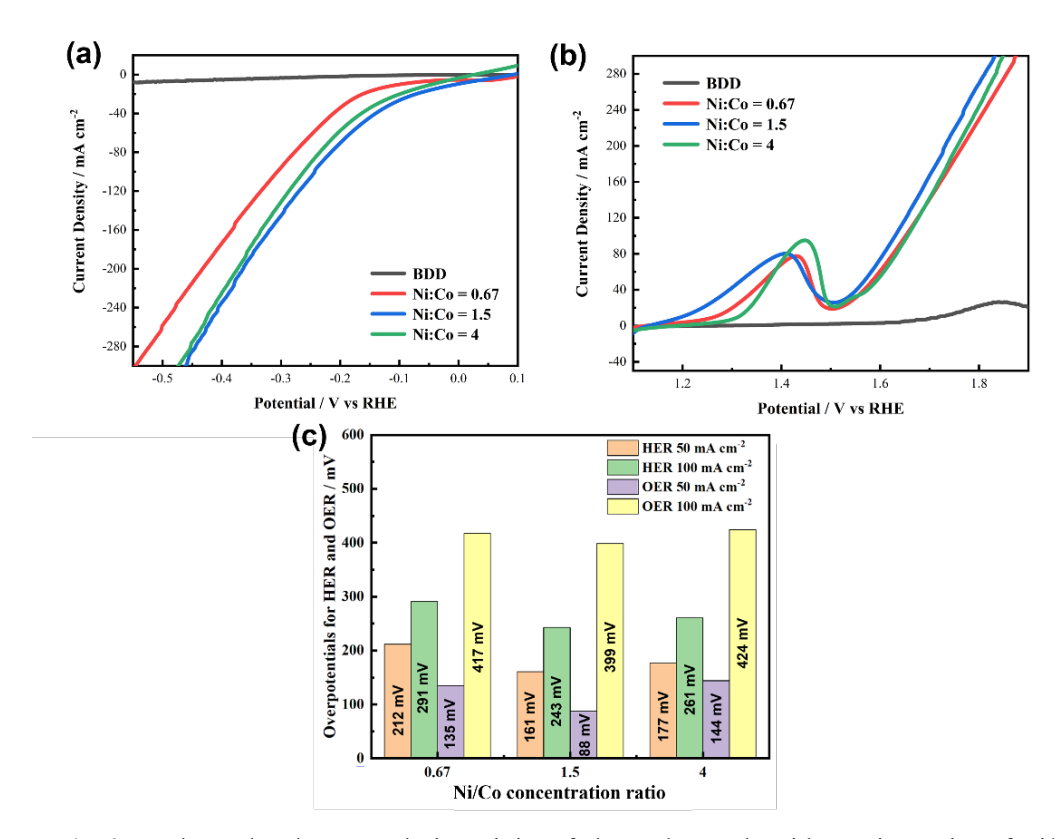


Fig. 2. Evaluate the electrocatalytic activity of electrodes made with varying ratios of Ni/Co concentration. (a-b) Plot the electrodes' overpotential at current densities of 50 mA cm⁻² and 100 mA cm⁻². (c) Linear sweep polarization curves obtained in 1 M KOH at a scan rate of 5 mV s⁻¹.

The NiCo precursor on BDD was made up of porous agglomerates that resemble island-like structures with the size range from 5 to 15 µm (Figs. 3g-h), contrasting sharply with the pristine BDD smooth pyramid surface (Figs. 3a-b). The apparent change in morphology proved the completion of the complexation of the NiCo structure on the BDD. In this work, we attempted to control the pore size and porosity of the NiCo layer by changing the content of ammonia to further improve the specific surface area of the electrode. During the depositions, the content of ammonia exhibited a significant effect on the morphology of the NiCo layers when a 3D porous morphology was prepared by the bubble dynamic template method (Figs. 3c-h). Three sets of experiments were designed with all other conditions held constant and ammonia levels of 5 %, 10 %, and 20 %. The pore size of the NiCo layer deposited at an ammonia level of 5 % was unevenly distributed and the surface of the spherical agglomerated particles was smooth (Figs. 3c-d). When the ammonia level increases to 10 %, the surface of the NiCo layer was distributed with pores of uniform size (25-40 μm). Compared with the ammonia level of 5 %, the boundaries between the spherical agglomerated particles obtained at the ammonia level of 10 % were obvious, and the surface of the particles becomes rough, which was conducive to increasing the active specific surface area and exposing more catalytic active site (Figs. 3e-f). Further increased the ammonia level to 20 %, a significant difference in the pore size was observed (Figs. 3g-h) even though the pore structure was uniformly distributed. Some of the pore diameters even reached 80 µm. It is clear that the surface morphology of the NiCo layer can be controlled by adjusting the ammonia level, and too high ammonia level promotes the rapid generation of bubbles, which in turn leads to an enlarged pore size.

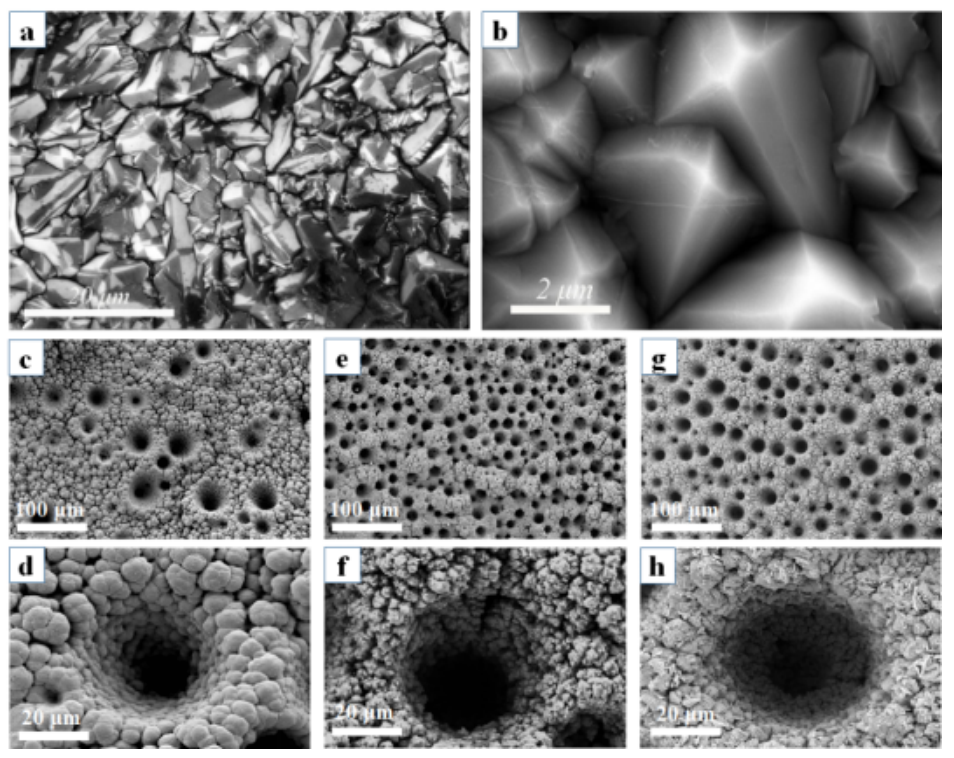


Fig. 3. (a-b) SEM images of pristine BDD, (c-h) Por-NiCo/BDD SEM plots deposited at the ammonia level of 5 %, 10 % and 20 %, respectively.

The performance of Por-NiCo/BDD electrodes regulated by ammonia levels was comprehensively analyzed in combination with electrochemical testing. Figs. 4a-c shows the CV curves of the Por-NiCo/BDD electrodes in 1 mol/L KOH solution at different sweep speeds in the range of 0-0.1 V versus Hg/HgO to investigate the variation of ammonia content on the electrochemical specific surface area (ESCA) of the plated 3D porous NiCo layers. A positive relationship exists between ESCA and C_{dl} values ($ESCA = A \cdot C_{dl}/C_s$, A: geometric area of the motor in cm², Cs: surface two-layer capacitance of an ideal flat electrode in μF cm⁻²) [4,11]. Fig. 4d shows the curves of the relationship between the current density difference ΔJ and the sweep speed (i.e., bilayer capacitance) converted from the CV curves for each electrode. The C_{dl} of the electrode deposited at the ammonia of 10 % is 1.894×10^{-5} mF cm⁻², which is about 2.29 times higher than of the 5 % (8.254 \times 10⁻⁶ mF cm⁻²) and about 1.75 times higher than that of 20 % (1.083 \times 10⁻⁵ mF cm⁻²). This resulting shows that the ESCA of the BDD electrode deposited at the ammonia of 10 % was improved compared with the other two groups, mainly due to the uniform distribution and the consistent pore size of the porous electrode surface. Further, the electrodes deposited

at the ammonia level of 10 % had the best catalytic activity with HER and OER overpotentials of 271 and 407 mV at 100 mA cm⁻², respectively, which were lower than those deposited a 5 % (306 and 454 mV) and 20 % (291 and 423 mV) (**Figs. 4e-f**). The good porous structure effectively increases the contact area between the electrolyte and the catalyst, which exposes more active sites, which is in line with SEM observation.

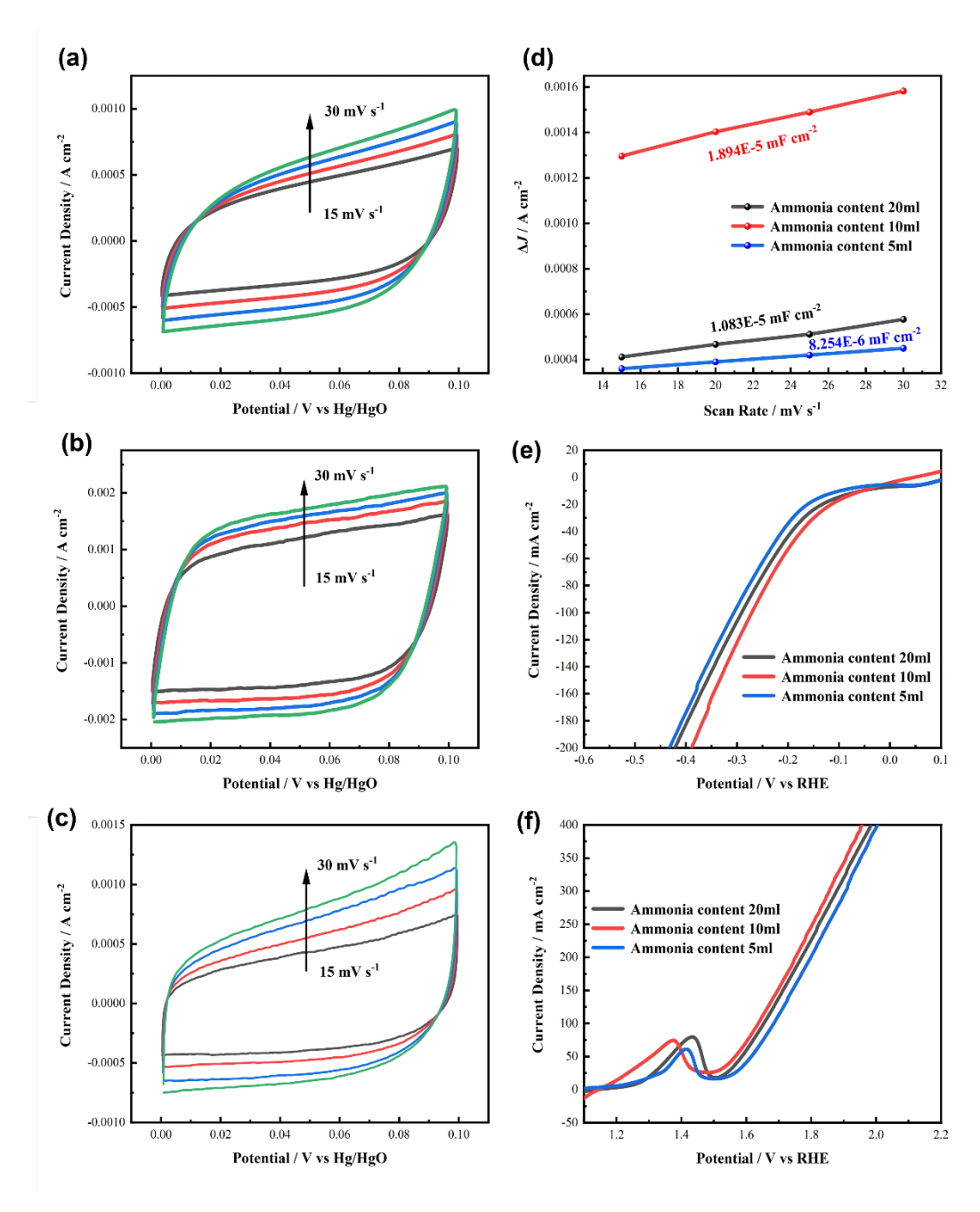


Fig. 4. Comparison of electrocatalytic performance of electrodes deposited at different ammonia level: (a-c) CV curves for Por-NiCo/BDD electrodes deposited at the ammonia of 5 %, 10 % and 2 0 % in 1 M KOH solution at different sweep speeds in the range of 0 to 0.1 V vs. Hg/HgO, (d) the

relationship curves between current density difference ΔJ and sweeping velocity, (e-f) linear sweep polarization curves acquired at a scan rate of 5 mV s⁻¹ in 1 M KOH.

The NiCoP layer obtained after phosphating treatment has a similar morphology to the NiCo layer, but more sheet structures grow on the agglomerated particles formed a cauliflower-like porous structure (Figs. 5a-f). High magnification SEM images reveal that the surface of NiCoP was rougher than that of the NiCo layer (Figs. 5c, f). CV test results show that the chemical specific surface area of Por-NiCoP/BDD electrode was much higher than that of Por-NiCo/BDD and BDD (Fig.6). The TEM images of Fig. 5g confirmed the existence of NiCo nanocubes with sizes of around 200 nm. Fig. 5h shows the presence of NiCoP nanosheets, revealed by the (111) and (110) crystal plane of NiCoP nanosheets corresponding to the lattice fringe spacings of 0.225 and 0.296 nm, respectively [26]. In the selected area electron diffraction (SAED) pattern of Por-NiCoP/BDD hybrids (Fig. 5i), the diffraction rings were basically consistent with the (111), (201), and (210) planes of NiCoP. Combining SEM and TEM evidence, a unique hierarchical cube-on-sheet structure was constructed. The EDS mappings demonstrated that the Co, Ni, and P elements were uniformly dispersed on the cauliflower-like agglomerate structure (Fig. 5j). Also, EDS confirmed that the deposited Por-NiCoP/BDD electrode had a designed Ni/Co atomic ratio of 1.44. The XRD patterns show that the deposited NiCo precursor is mainly composed of Ni, Co, and Ni-Co alloy (Fig.5I) [27]. The NiCoP phase was generated after phosphating, which was consistent with the literature report [28-30]. XRD result confirmed the coexistence of NiCoP and NiCo in Por-NiCoP/BDD, which verified the speculation that NiCoP grew on NiCo layer and corroborated the SEM and TEM results.

Table 1. Surface elemental content analysis of Por-NiCoP/BDD samples (from Fig. 5k).

Elemental	wt%	At%
В	1.42	5.64
C	5.12	18.32
P	11.93	16.53
Co	38.95	24.38
Ni	42.58	35.13
Overall amount	100.00	100.00

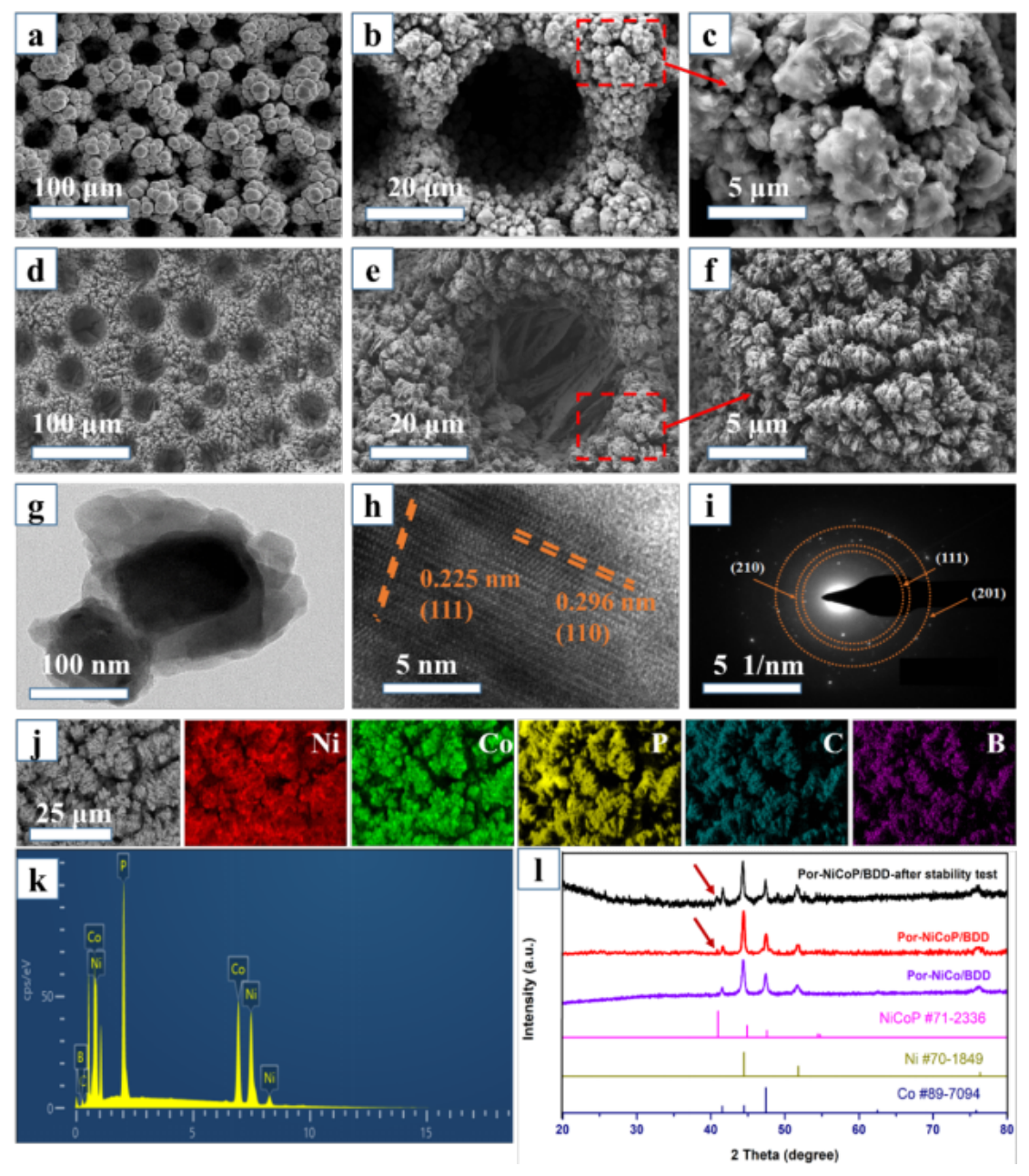


Fig. 5. (a-c) Por-NiCo/BDD SEM pictures at varying magnifications, (d-f) Por-NiCoP/BDD SEM pictures at varying magnifications, and (g) TEM image, (h) HRTEM images, and (i) SAED pattern of the obtained Por-NiCoP/BDD, (j-k) EDS mappings of Por-NiCoP/BDD and (l) XRD pattern.

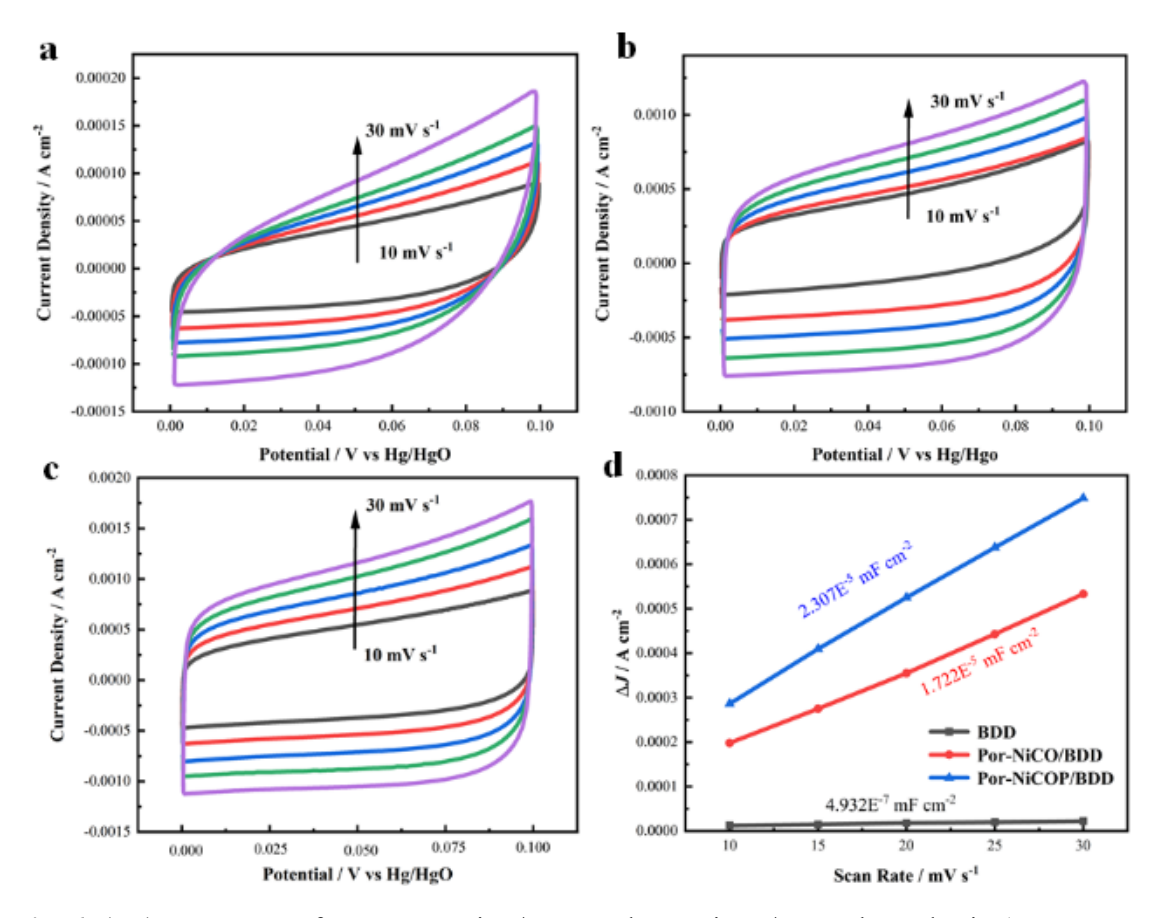


Fig. 6. (a-c) CV curves of BDD, Por-NiCo/BDD and Por-NiCoP/BDD electrodes in 1 M KOH solution at different sweep speeds in the range of $0\sim0.1$ V vs. Hg/HgO, (d) and curves of the relationship between current density difference ΔJ and sweeping velocity.

The element types and elemental chemical states of the deposited NiCoP layer were ascertained using the XPS analyzer. From the NiCoP surface, the elements Ni, P, C, Na, O, and Co were identified between 0 and 1000 eV. (**Fig. 7a**). Among the elements, Ni, Co, and P were assigned to Por-NiCoP/BD. Na came from the residues of the NaH₂PO₂·H₂O phosphating treatment, while the presence of O was due to the oxidation of P in the atmosphere [31]. The binding energies of the Ni 2p_{3/2} splitting peaks were mainly clustered at 870.0 and 852.8 eV, which was due to the Ni-P bond in NiCoP species (**Fig. 7c**) [32]. The binding energies of the Ni-O bonds were verified at the splitting slits 874.2 and 856.4 eV [32]. The satellite peaks were then located at 880.0 and 861.5 eV [33]. The two splitting peaks of Co 2p at 793.2 and 778.6 eV were derived from the Co-P bonds of the CoNiP phase (**Fig. 7b**) [34-35]. The binding energies of 796.2 and 782.6 eV originate from the splitting slit of Co 2p_{1/2}, corresponding to the Co-O bond [36]. The Ni/Co-O bonds were resulted from the

superficial oxidation of bimetallic phosphide NiCoP when it isexposed in the air condition [7]. The P 2p spectrum shows two obvious peaks at 129.2 and 133.2 eV, corresponding to the metal phosphides bond and phosphate species (PO_4^{3-}), respectively (Fig.7d) [27]. The binding energy of 129.2 eV negatively shifted from elemental P (130.0 eV), suggesting that P atom carries partly negative charge ($P^{\delta-}$) [38]. Therefore, the P atom possesses the ability of trapping positive charge H* during HER reaction. Moreover, the formation of phosphate species (PO_4^{3-}) is caused by partial oxidation of the surface exposed to air, which is consistent with the previous researches [28,39].

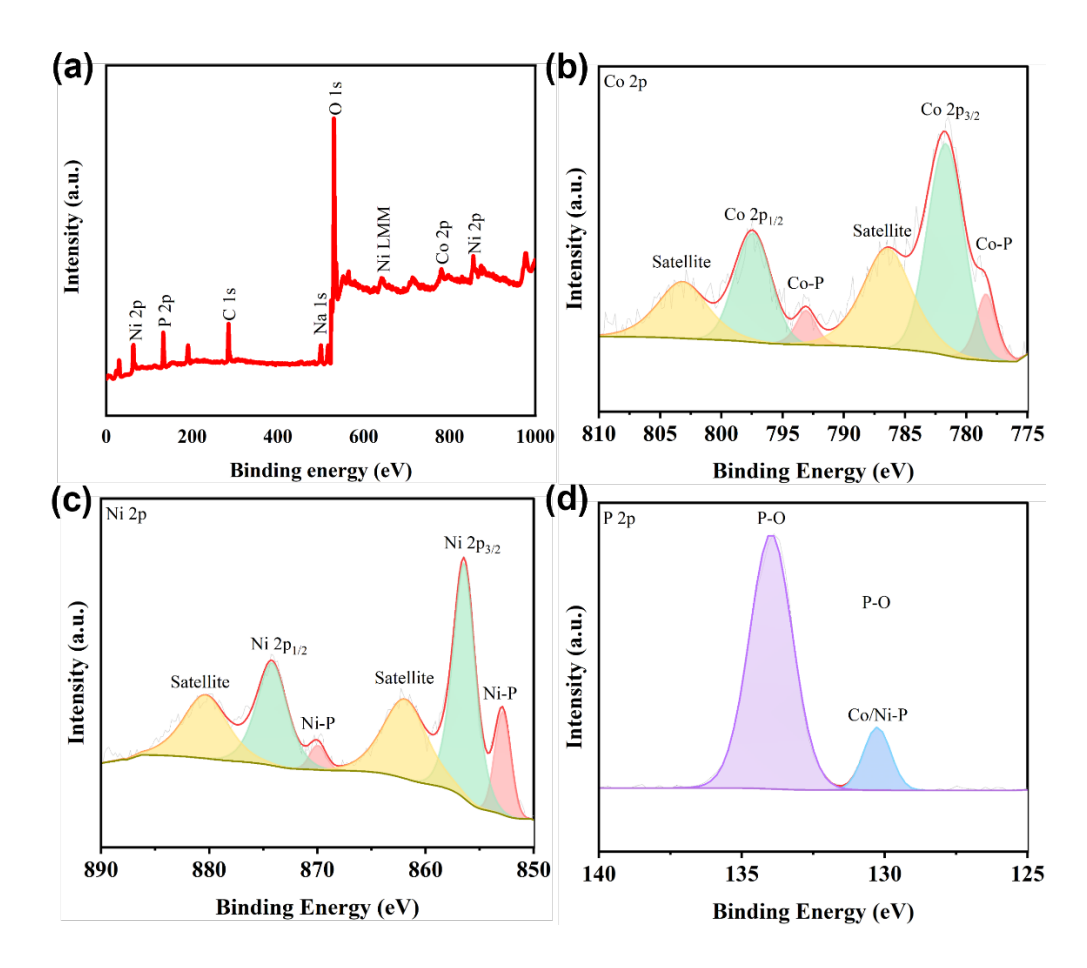


Fig. 7. (a) XPS spectra of Por-NiCoP/BDD, and the corresponding (b) Co 2p, (c) Ni 2p, and (d) P 2p spectra.

The HER catalytic activity tests for each phase of the samples were conducted in 1 M KOH solution or alkaline-simulated seawater (referred to as alkaline-simulated seawater unless otherwise specified) containing a mixture of 1 M KOH and 3.5% NaCl. The solution was passed through N₂ for a period of about 20 min prior to each

test to prevent the interference of dissolved oxygen. Fig. 8a shows the back-swept LSV curves of the pristine BDD, Por-NiCo/BDD, and Por-NiCoP/BDD electrodes in 1 M KOH solution and alkaline-simulated seawater (labeled as Por-NiCoP/BDD-sea in the Fig.8), at the sweep speeds of 5 mV s⁻¹. The pristine BDD electrode showed almost no HER performance, and the overpotential of the Por-NiCo/BDD electrode at a current density of 100 mA cm⁻² corresponded to 271 mV. Meanwhile, the overpotentials of the phosphatized Por-NiCoP/BDD electrode in 1 mol/L KOH solution and alkaline-simulated seawater at 100 mA cm⁻² reduced to 239 and 261 mV, respectively. The result suggested that the phosphatization of Ni-Co transition metals helped in promoting the HER reaction, especially at high current densities. The Tafel curve for HER, transformed from the LSV curve in Fig. 8a, was shown in Fig. 8b. The Tafel slope value of 68.55 mV dec⁻¹ for the Por-NiCoP/BDD electrode in the 1 M KOH solution was calculated by linear fitting, which was better than 97.41 mV dec-1 in alkaline-simulated seawater and significantly better than 123.57 mV dec-1 for the Por-NiCo/BDD electrode 1 M KOH solution. This finding suggested that the phosphatization of Ni and Co also contributed to the HER kinetic reactivity of the electrode. The main reason for the increase in its HER reactivity was potentially the increase in the ESCA of the sample due to the transition metal phosphatization (Fig.6). Meanwhile, the addition of NaCl slightly decreased the HER catalytic activity. The actual picture of the HER test device was shown in Fig. 8c, where a large number of gas bubbles can be clearly seen generated on the working electrode and quickly detach from the electrode, moving upward until they escape from the surface of the solution. The charge transfer kinetics at the electrode/electrolyte interface of the electrodes was explored by electrochemical impedance spectroscopy (EIS) under the test conditions of -1.1 V versus Hg/HgO and in the frequency ranging 10 kHz to 0.01 kHz. The EIS curves of the BDD, Por-NiCo/BDD, and Por-NiCoP/BDD electrodes in 1 M KOH solution and alkaline-simulated seawater were shown in Fig. 8d. The Nyquist semicircle of the Por-NiCoP/BDD electrodes is the smallest in the 1 M KOH solution, indicating that it has the smallest resistance to charge transfer (Rct) and the fastest rate of charge transfer in the HER process under this condition.

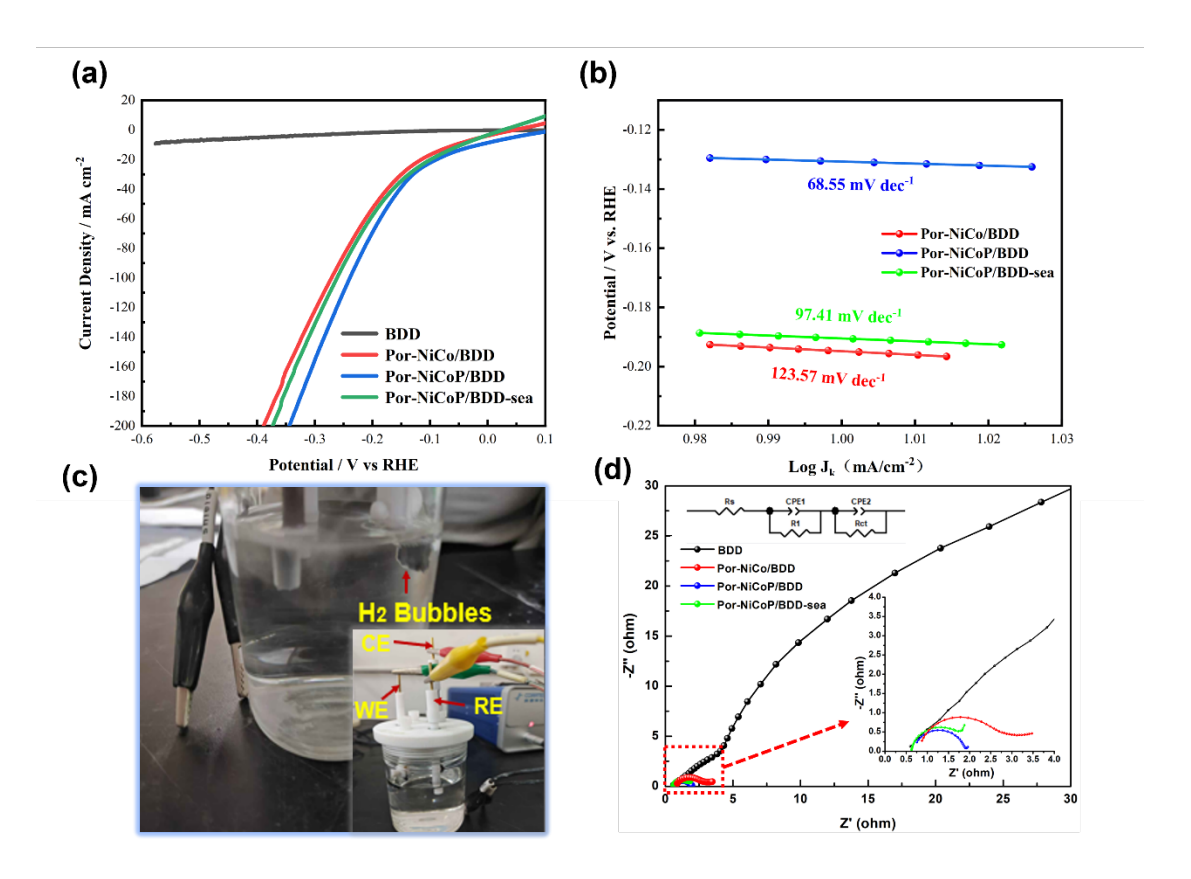


Fig. 8. For each electrode (a) LSV backscan curve at a sweep rate of 5 mV s⁻¹ in 1 M KOH solution or alkaline-simulated seawater, (b) Tafel curve corresponding to a current density of 10 mA cm⁻², (c) the actual picture of HER test devices, (d) EIS curve at a potential of -1.1 V vs Hg/HgO.

The OER catalytic activity analyses of each electrode were also performed in 1 M KOH solution or alkaline-simulated seawater. The solution was treated with O₂ passage for a duration of about 20 min before each test to saturate the solution with oxygen and reduce the effect caused by the insufficient oxygen content of the solution during the test. **Fig. 9a** shows the back-swept LSV curves of the pristine BDD, Por-NiCo/BDD, and Por-NiCoP/BDD electrodes in 1 M KOH solution and alkaline-simulated seawater (labeled as Por-NiCoP/BDD-sea in the **Fig.9**), at the sweep speeds of 5 mV s⁻¹. The pristine BDD electrode lacks OER activity, while the Por-NiCo/BDD electrode has an OER overpotential of 426 mV at the current density of 100 mA cm⁻² in 1 M KOH solution and exhibits OER activity. The OER overpotential of the Por-NiCoP/BDD electrode was further reduced to 328 and 400 mV at 100 mA cm⁻² in 1 M KOH solution and alkaline-simulated seawater, respectively. This finding suggested that transition metal phosphatization helps in promoting further reduction of the OER

overpotential, especially at high current densities where the decreasing trend of the overpotential was evident. The OER overpotential was increased to a certain extent by the competition of the Cl- ion precipitation chlorine reaction, as evidenced by the difference in the performance of the OER of the Por-NiCoP/BDD electrode in 1 M KOH solution versus alkaline-simulated seawater. The Tafel slope value of the Por-NiCoP/BDD electrode was 67.72 mV dec-1 in 1M KOH solution, which was better than 73.71 mV dec⁻¹ in alkaline-simulated seawater and significantly better than 81.44 mV dec⁻¹ for the Por-NiCo/BDD electrode. The actual picture of the OER test device was shown in Fig. 9c, where the gas bubbles can be clearly seen generated on the working electrode and quickly detach from the electrode, moving upward until they escape from the surface of the solution, which means that water-splitting occurs on the electrode. This electrochemical test determined that phosphating contributed to the OER kinetic reactivity of the electrode, which originated from the synergistic action of the Ni-Co oxide converted in-situ on the surface of NiCoP with the remaining highly conductive NiCoP in the interior [36, 40]. The EIS results confirmed the resistance of Por-NiCoP/BDD electrode in 1 M KOH solution is the smallest, indicating that it has the smallest Rct and the fastest charge-transfer rate in the OER process (Fig.9d). The Cl⁻ in the solution hinder the reaction process of OER, making the electrode less active. Even so, the deposited Por-NiCoP/BDD electrode in this work is still attractive compared with other related seawater electrolysis electrodes (Table 2).

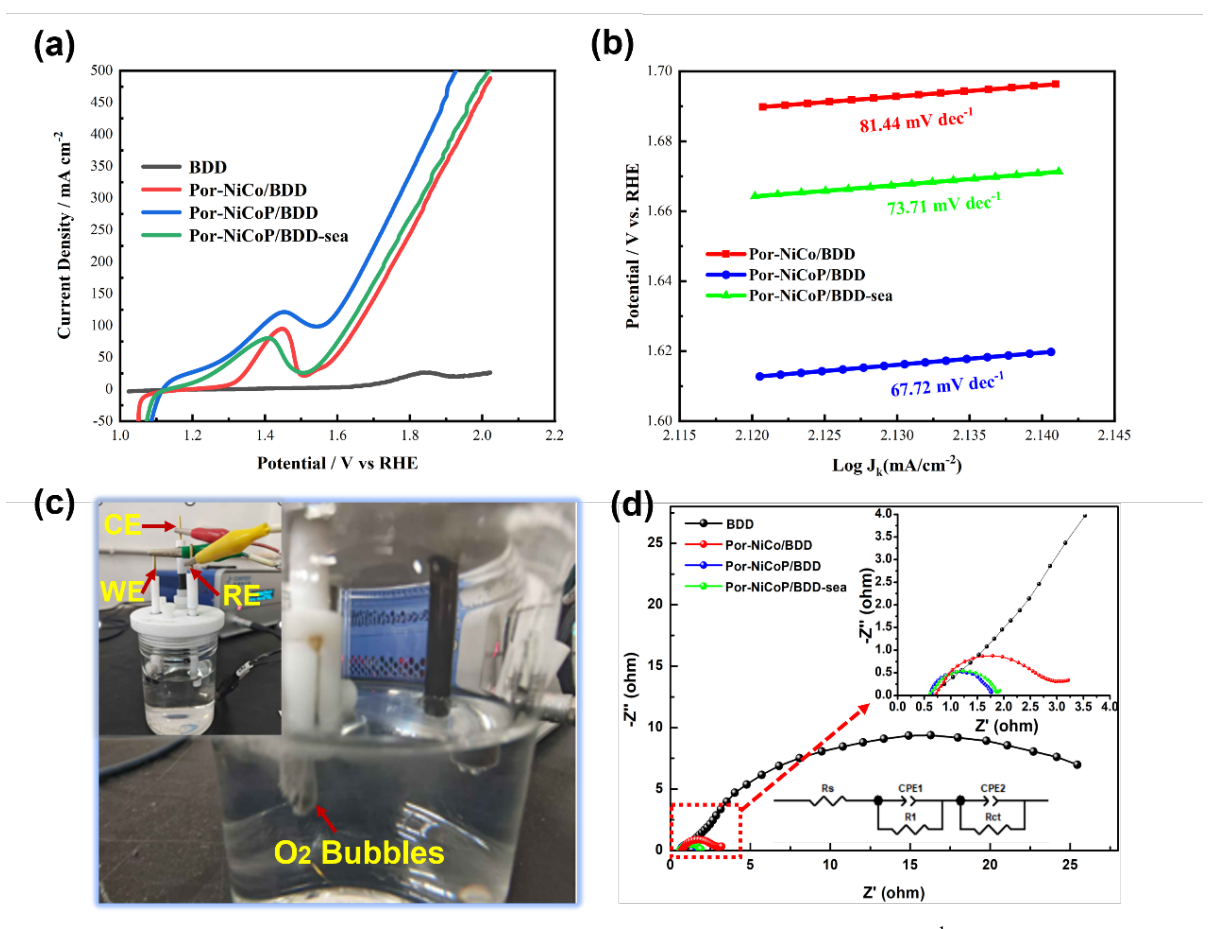


Fig. 9. For each electrode (a) LSV backscan curve at a sweep rate of 5 mV s⁻¹ in 1 M KOH solution or alkaline simulated seawater, (b) Tafel plots, (c) the actual picture of OER test devices, (d) EIS curve at a potential of 0.6 V vs Hg/HgO.

Table. 2. Activity indexes of OER/HER electrocatalysts containing Ni-Co-P and other related catalysts.

Catalyst	Electrolytes	Electrodes	Overpotential @100 mA cm ⁻² (mV)	Tafel Slope (mV dec ⁻¹)	Ref.
Por-NiCoP	1.0 M KOH	BDD	HER 239 OER 328	68.6 67.7	This work
NiCoP-Se	1.0 M KOH	Nickel Foam (NF)	OER 412	87.2	[4]
Ni_2P	1.0 M KOH	NF	HER 252	92.0	[6]
$Ni_{12}P_5$	1.0 M KOH	NF	HER 393 OER 360	/	[12]
CoP_2	1.0 M KOH	NF	HER 420 OER 523	85.6 82.5	[22]
$Co_{3-x}Pd_xO_4$	1.0 M KOH + 0.5 M NaCl	NF	OER 586	60.3	[30]
CoNiP/Co _x P	1.0 M KOH	NF	HER 257	70.0	[27]
NiCo	0.5 M H ₂ SO ₄	NF	HER 274	81.2	[41]

The chrono-current (i-t) method was used in alkaline-simulated seawater to investigate the catalytic stability of HER and OER of the Por-NiCoP/BDD-sea

electrode materials. During the HER and OER processes, the current density of the Por-NiCoP/BDD-sea electrode decayed to 95.94 % and 98.48 % of the original current density of 100 mA cm⁻² for 50 h stability testing, respectively (Figs.10a, c). The HER overpotential increased from 256 mV to 273 mV before and after the stability testing (Figs.10b). Fig. 10 d depicts the increase of the OER overpotential from 399 mV before the test to 406 mV after the test. In addition, EIS testing is a valuable method to evaluate the stability of the catalytic layer [42]. The EIS information before and after the stability test was recorded. There was only a small increase in Rct after 50 h of testing (Figs. 10e, f), which showed the stability of the NiCoP catalyst layer. The surface morphology and microstructure of Por-NiCoP/BDD-sea after stability testing were shown in Fig. 11. It can be observed that the electrode surface was encapsulated with a thin film, and magnification revealed that the overall architecture with porous morphology was not destroyed (Figs. 11a-c). As shown in Figs. 11d and g, EDS analysis of the film coated on the catalyst surface reveals that the elements K, Cl, Na, and O are newly introduced. These elements were attached to the catalyst surface by electrolysis and oxidation reactions when the electrode works in the electrolyte. Combined with HRTEM and SAED analyses (Figs. 11e, f and h), the lattice fringes and diffraction rings are almost unchanged, proving that the microstructure of the NiCoP catalyst has not been destroyed for 50h, which highlights the structure stability of the Por-NiCoP/BDD-sea electrode. This was also emphasized by the XRD patterns after stability testing (Fig.5I). The Por-NiCoP/BDDsea electrode with BDD as the substrate exhibits high OER stability mainly because the highly stabilized BDD resist the corrosion of Cl⁻ ions, ensuring that the collector of the electrode will not be fractured. Long-term electrochemical tests revealed interesting performance stability of the deposited Por-NiCoP/BDD-sea electrode.

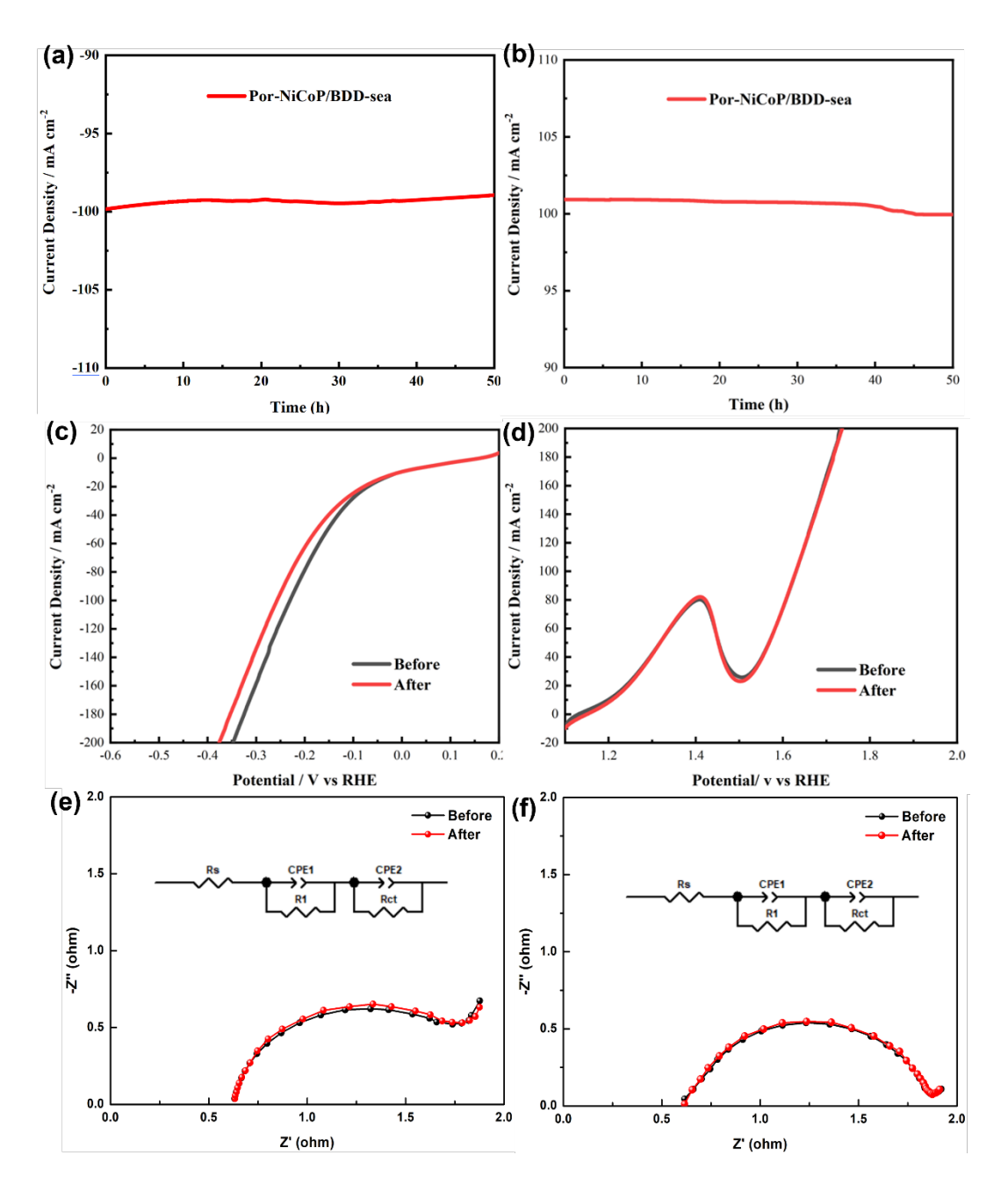


Fig.10. Por-NiCoP/BDD in alkaline-simulated seawater containing 1 M KOH and 3.5 wt % NaCl: (a, b) chrono-current method curves; (c, d) back-sweep LSV curves before and after stabilization at a sweep rate of 5 mV s⁻¹; (e, f) EIS curves at a potential of -1.1 V vs Hg/HgO and 0.6 V vs Hg/HgO before and after stabilization at a sweep rate of 5 mV s⁻¹.

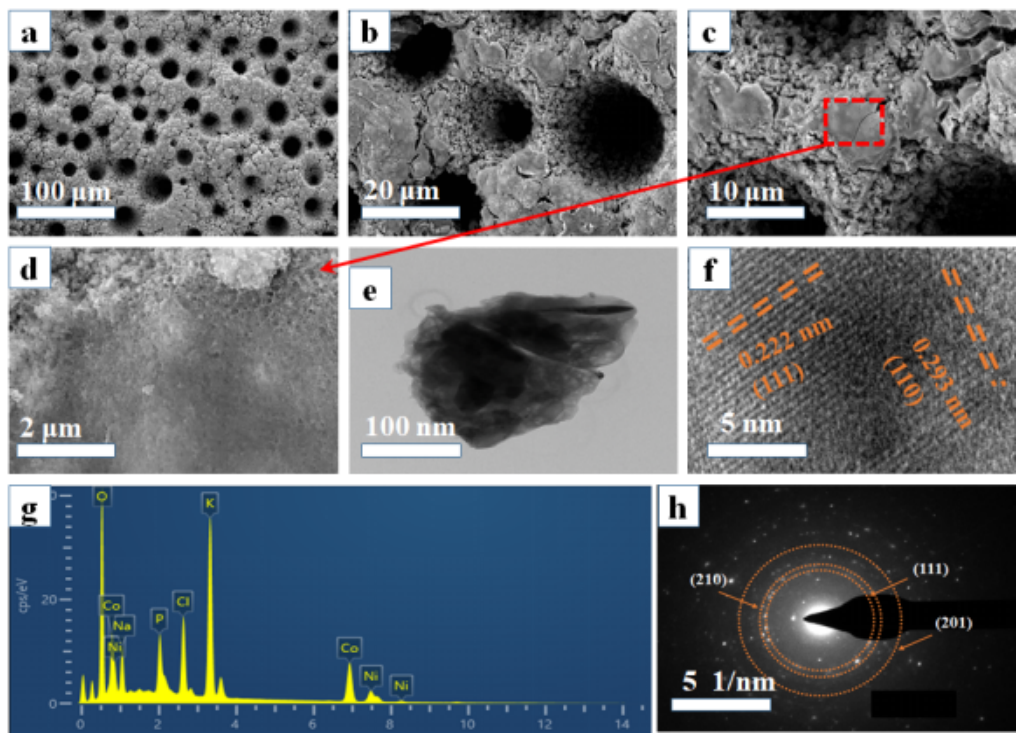


Fig. 11. (a-d) SEM images of Por-NiCoP electrode after stability testing, and corresponding (e-f, h) TEM images and (g) EDS energy spectra.

4. Conclusion

In conclusion, Por-NiCoP/BDD electrodes with controllable 3D porous morphology for seawater electrolysis were deposited through electrodeposition combined with bubble dynamic template methods. The optimal Ni/Co atomic ratio of 1.5:1 and ammonia level of 10 % were determined to regulate the 3D porous morphology to promote the Por-NiCoP/BDD electrode electrocatalytic performance. As prepared Por-NiCoP/BDD-sea electrode showed good catalytic activity in alkaline-simulated seawater because of the 3D porous morphology provides huge specific surface area and high catalytic activity of metal phosphides. The OER and HER overpotential of Por-NiCoP/BDD-sea electrode in alkaline-simulated seawater were 400 and 261 mV, respectively, at a current density of 100 mA cm⁻². Alkaline-simulated seawater electrolysis for 50 h revealed interesting catalytic properties and structural stability of the electrode. The OER and HER overpotentials of the electrode decayed by only 1.52 % and 4.06 %, respectively, after stability testing for 50 h. The high stability of the BDD substrate was emphasized (i.e., the BDD acts as an intact fluid collector to ensure that the electrodes properly work even after the outer layer of

Ni has been completely corroded). This work provides a valuable reference for the design of seawater electrolysis electrodes.

Author contributions

Xiaolei Ye: methodology, formal analysis, investigation, data curation and writing - original draft. Genjie Chu: formal analysis and writing - review & editing. Jiyun Gao: formal analysis. Ming Hou: investigation, formal analysis, writing - review & editing. Shenghui Guo: funding acquisition, supervision. Ziqi Zhou: formal analysis. Mingxu Li: formal analysis. YunChuan Li: software. Li Yang: conceptualization, funding acquisition, supervision. Pascal Briois: language review, formal analysis and visualization.

Acknowledgements

This research was supported by National Natural Science Foundation of China (52364051, 52374389); The authors (Li Yang, Shenghui Guo) would like to acknowledge Xing Dian talent support program of Yunnan Province.

Conflict of Interest

The authors declare no conflict of interest.

References

- [1] X. Tian, X. Lu, B. Xia, et al. Advanced Electrocatalysts for the Oxygen Reduction Reaction in Energy Conversion Technologies [J], Joule, 4 (2020) 45-68.
- [2] Y. Yang, Y. Yu, J. Li, et al. Engineering Ruthenium-Based Electrocatalysts for Effective Hydrogen Evolution Reaction [J], Nano-Micro Letters, 13 (2021).
- [3] D. Bak, J. Kim, Facile fabrication of pseudo-microspherical ZnO/CdS core-shell photocatalysts for solar hydrogen production by water splitting, Ceramics International, 43 (2017) 13493-13499.
- [4] R. He, J. Li, L. Feng. NiCoP selenization for enhanced oxygen evolution reaction in alkaline electrolyte [J], Catalysis Communications, 163 (2022).
- [5] M. Yang, T. Feng, Y. Chen, et al. Synchronously integration of Co, Fe dual-metal

- doping in Ru@C and CDs for boosted water splitting performances in alkaline media [J], Applied Catalysis B-Environmental, 267 (2020).
- [6] G. Qu, Y. Zhao, G. Zhou, Y. Cai, S. Kang, Y. Xu et al. Ultrahigh length-to-diameter ratio nickel phosphide nanowires as pH-wide electrocatalyst for efficient hydrogen evolution [J], Electrochimica Acta, 298 (2019) 943-949.
- [7] N. Reddy, U. Bharagav, M. Kumari, K. Cheralathan, P. Ojha, M. Shankar, S. Joo, Inclusion of low cost activated carbon for improving hydrogen production performance of TiO₂ nanoparticles under natural solar light irradiation, Ceramics International, 47 (2021) 10216-10225.
- [8] C. Huang, T. Ouyang, Y. Zou, et al. Ultrathin NiCo₂P_x nanosheets strongly coupled with CNTs as efficient and robust electrocatalysts for overall water splitting [J], Journal of Materials Chemistry A, 6 (2018) 7420-7427.
- [9] Z. Wang, H. Wang, S. Ji, X. Wang, R. Wang, et al. Hollow-structured NiCoP nanorods as high-performance electrodes for asymmetric supercapacitors [J], Materials & Design, 193 (2020) 108807.
- [10] X. Hang, Y. Xue, J. Zhao, R. Yang, H. Pang, et al. In situ generation of NiCoP nanoparticles on a bimetal-organic framework for high-performance supercapacitors[J], Inorganic Chemistry, 27 (2022) 10435-10441.
- [11]L. Wu, L. Yu, F. Zhang, B. Mcelhenny, et al. Heterogeneous Bimetallic Phosphide Ni₂P-Fe₂P as an Efficient Bifunctional Catalyst for Water/Seawater Splitting [J], Advanced Functional Materials, 31 (2021).
- [12] P. Menezes, A. Indra, C. Das, C. Walter, M. Driess, et al. Uncovering the nature of active species of nickel phosphide catalysts in high-performance electrochemical overall water splitting, Acs Catalysis, 7 (2017) 103-109.
- [13] P. Gan, A. Pal, S. Rivi, N. Kumari, et al. Tuneable and coral-like NiCoP for enhanced oxygen and hydrogen evolution reaction [J], Materials Today Communications, 38 (2024) 108063.
- [14] Y. Wu, Y. Xu, Y. Zhang, J. Feng, X. Cheng, et al. Fabrication of NiCoP decorated TiO₂/polypyrrole nanocomposites for the effective photocatalytic degradation of tetracycline [J], Chinese Chemical Letters, 33 (2022) 2741-2746.

- [15]T. Jiang, X. Jiang, V. Kyriakou, et al. Deep reconstruction of Ni-Al-based precatalysts for a highly efficient and durable anion-exchange membrane (AEM) electrolyte [J], Journal of Materials Chemistry A, 11 (2023) 26011-26022.
- [16] R. Wu, B. Xiao, Q. Gao, et al. A janus nickel cobalt phosphide catalyst for high-efficiency neutral pH water splitting [J]. Angewandte Chemie, 130(47) (2018) 15671-15675.
- [17]H. Feng, L. Tang, G. Zeng, et al. Electron density modulation of Fe_{1-x}Co_xP nanosheet arrays by iron incorporation for highly efficient water splitting [J], Nano Energy, 67 (2020).
- [18] C. Du, L. Yang, F. Yang, et al. Nest-like NiCoP for Highly Efficient Overall Water Splitting [J], Acs Catalysis, 7 (2017) 4131-4137.
- [19] Y. Xu, H. Lv, H. Lu, Q. Quan, W. Li, X. Cui, et al. Mg/seawater batteries driven self-powered direct seawater electrolysis systems for hydrogen production [J], Nano Energy 98 (2022) 107295.
- [20] J. Zhang, L. Zhang, X. Wang, et al. A hierarchical hollow-on-hollow NiCoP electrocatalyst for efficient hydrogen evolution reaction [J], Chemical Communications, 56 (2020) 90-93.
- [21] L. Hu, X. Tan, X. Yang, et al. Electrolysis of Direct Seawater: Challenges, Strategies, and Future Prospects [J], Chinese Journal of Chemistry, 41 (2023) 3484-3492.
- [22] Z. Yu, L. Liu. Recent Advances in Hybrid Seawater Electrolysis for Hydrogen Production [J], Advanced Materials, 36 (2023) 2308647.
- [23] J. Zhu, L. Hu, P. Zhao, et al. Recent Advances in Electrocatalytic Hydrogen Evolution Using Nanoparticles [J], Chemical Reviews, 120 (2020) 851-918.
- [24] K. Zhang, K. Zhang, Y. Ma, et al. Construction of Z-Scheme TiO₂/Au/BDD Electrodes for an Enhanced Electrocatalytic Performance [J], Materials, 16 (2023).
- [25]Z. Geng, Z. Cui, Y. Liu, et al. Electrodeposition ZnO/BDD film as a supercapacitor electrode [J], Diamond Related Materials, 140 (2023).
- [26] Y. Liu, D. Jiang, J. Zhu, Y. Lu, C. Liu, S. Xu. Facile synthesis of hierarchical nicop nanosheets/nicop nanocubes homojunction electrocatalyst for highly efficient

- and stable hydrogen evolution reaction [J], Applied Surface Science, (2021) 150537.
- [27]D. Liu, H. Ai, M. Chen, P. Zhou, B. Liu, D. Liu, X. Du, et al. Multi-phase heterostructure of CoNiP/Co_xP for enhanced hydrogen evolution under alkaline and seawater conditions by promoting h₂o dissociation [J], Small, 17 (2021) 2007557.
- [28] Q. Lv, J. Han, X. Tan, et al. Featherlike NiCoP holey nanoarrys for efficient and stable seawater splitting [J]. ACS Applied Energy Materials, 2(5) (2019) 3910-3917.
- [29] L. He, Z. Cai, D. Zheng, et al. Three-dimensional porous NiCoP foam enabled high-performance overall seawater splitting at high current density [J]. Journal of Materials Chemistry A, 12(5) (2024) 2680-2684.
- [30] Y. Yang, R. Zhou, J. Gan, et al. Integrating electrocatalytic seawater splitting and biomass upgrading via bifunctional nickel cobalt phosphide nanorods [J]. Green Chemistry, 25(10) (2023) 4104-4112.
- [31]Z. Hou, Y. Zhu, W. Du, et al. Nano-control synthesis the porous network of NiCoP and F doped NiC₂Al-LDHs@ZnFeAl-LDHs nanosheets as superior catalyst for efficient overall water splitting [J], Journal of Industrial and Engineering Chemistry, 112 (2022) 85-95.
- [32] Q. Zong, H. Yang, Q. Wang, Q. Zong, et al. NiCo₂O₄/NiCoP nanoflake-nanowire arrays: a homogeneous hetero-structure for high performance asymmetric hybrid supercapacitors [J], Dalton Transactions, 47 (2018)16320-16328.
- [33] D. Li, C. Liu, W. Ma, et al. Fe-doped NiCoP/Prussian blue analog hollow nanocubes as an efficient electrocatalyst for oxygen evolution reaction [J], Electrochimica Acta, 367 (2021).
- [34] T. Wang, X. Cao, L. Jiao. Ni₂P/NiMoP heterostructure as a bifunctional electrocatalyst for energy-saving hydrogen production [J], eScience, 1 (2021) 69-74.
- [35]X. Luo, P. Ji, P. Wang, et al. Interface engineering of hierarchical branched modoped $Ni_3S_2/Ni_x/P_y$ hollow heterostructure nanorods for efficient overall water splitting [J], Advanced Energy Materials, 10 (2020).
- [36] N. Wang, P. Ou, S. Hung, J. Huang, A. Ozden, J. Abed, et al. Strong-proton-adsorption co-based electrocatalysts achieve active and stable neutral seawater splitting [J], Advanced Materials, 35 (2023).

- [37] B. You, N. Jiang, M. Sheng, et al. Hierarchically porous urchin-like Ni2P superstructures supported on nickel foam as efficient bifunctional electrocatalysts for overall water splitting [J]. Acs Catalysis, 6(2) (2016) 714-721.
- [38] Y. Shi, B. Zhang, Recent advances in transition metal phosphide nanomaterials: synthesis and applications in hydrogen evolution reaction [J]. Chemical Society Reviews, 45(6) (2016) 1529-1541.
- [39] Y. Li, J. Liu, C. Chen, et al. Preparation of NiCoP hollow quasi-polyhedra and their electrocatalytic properties for hydrogen evolution in alkaline solution [J]. ACS applied materials & interfaces, 9 (7) (2017) 5982-5991.
- [40]L. Yang, L.T. Huang, Y.H. Yao, et al. In-situ construction of lattice-matching NiP₂/NiSe₂ heterointerfaces with electron redistribution for boosting overall water splitting [J], Applied Catalysis B: Environmental, 282 (2021).
- [41] F. Yang, Z.L. Li, F. Zhu, et al. Three-dimensional multi-channel structure NiCo alloy used for boosting efficient overall water splitting [J], Fuel, 364 (2024).
- [42] N. Esfandiari, M. Aliofkhazraei, A.N. Colli, et al. Metal-based cathodes for hydrogen production by alkaline water electrolysis: Review of materials, degradation mechanism, and durability tests [J], Progress in Materials Science, 144 (2024) 101254.

Graphical abstract

